

Table of Contents

Supplementary Note 1	Hyperspectral noise modelling
Supplementary Note 2	Training data and data collection guidelines
Supplementary Note 3	Evaluation metrics
Supplementary Note 4	Model network interpretation
Supplementary Note 5	Calculating signal-to-noise ratio of hyperspectral images
Supplementary Note 6	Calculating effective photons from CCD readings
Supplementary Note 7	Deriving ground truth of PL spectrum in micro-PL mapping
Supplementary Figure 1	Effect of background noise levels in human visual signal detection of small features
Supplementary Figure 2	Hyperspectral microscopy of CsPbBr ₃ perovskite nanoplatelets
Supplementary Figure 3	Hyperspectral microscopy of CsPbBr ₃ perovskite nanosheets
Supplementary Figure 4	Effect of 1D Gaussian filter on local-PL spectra of wide-gap FA _{0.7} Cs _{0.3} Pb(I _{0.6} Br _{0.4}) ₃ perovskite films
Supplementary Figure 5	Curve fitting for EL maps of mixed Br/Cl blue perovskite LEDs
Supplementary Table 1	Evaluation of model generalizability with different number of channels of the input image
Supplementary Table 2	Effect of training data percentage on denoised image quality and accuracy metrics
Supplementary Table 3	Effect of patch size on denoised image quality and accuracy metrics
Supplementary Table 4	Evaluation on blind denoising processing speed for each method with various input image size

Supplementary Note

Supplementary Note 1: Hyperspectral noise modelling

The real noise distribution of a hyperspectral image contains a mixture of signal independent noise and signal dependent noise¹. Signal-independent noise is mainly thermal noise and read-out noise, and can be modelled by spectral-uncorrelated additive Gaussian noise. Signal-dependent noise is mainly photon (shot) noise which can be modelled by Poisson statistics.

Thermal noise results from vibrations of a large number of electrons in the detector, where the vibration of any electron is independent of that of another, and each electron contributes to a small part of the sum². Thus, thermal noise satisfies the central limit theorem³ of Gaussian distribution and can be modelled by additive Gaussian noise that follows a normally-distributed probability density function

P_{Gaussian}

$$p_{\text{Gaussian}}(x) = \frac{1}{\sigma\sqrt{2\pi}} e^{-\frac{(x-\mu)^2}{2\sigma^2}}$$

where x represents the brightness of the pixel, μ is the mean brightness, and σ^2 is the standard deviation. The range of x for an ideal normal distribution is $-\infty < x < \infty$. However, in practice, pixels in images have a defined value range, and any values that exceed the value range will be automatically truncated before being saved into the image file.

Photon (shot) noise occurs as most of the digital images are captured using charge-coupled device (CCD) cameras that convert incoming photons into electron charges at the semiconductor-oxide interface. Electron charges are discrete in nature, thus the distribution of photon counting noise is usually modelled as Poisson with parameter λ

$$P_{\text{Poisson}}(x = k) = \frac{e^{-\lambda}\lambda^k}{k!}$$

where $k = 0, 1, 2, \dots$ and λ is the expected number of photons per unit time interval. When λ is large (i.e. a lot of photons are received by the camera), the central limit theorem can be invoked and the Poisson distribution can be well approximated as the Gaussian distribution with both μ and σ^2 equal to λ .

Other noise: Pixels may sometimes have extremely high counts due to cosmic rays hitting the camera sensor. This is usually referred to as salt and pepper noise, which means only a few pixels are noisy, but they are extremely noisy, just like someone sprinkles white and black dots on the image. The detection probability of cosmic rays in microscopy is low because the exposure and area of the detector are significantly smaller than that of telescopes⁴. Although the amount of salt and pepper noise generated by cosmic rays is typically very low and can often be negligible during noise modeling, a carefully designed data normalization strategy is necessary to achieve good denoising results. This is because the influence of cosmic rays will lead to several pixels with extremely high counts, and thus create abnormal data distribution during data normalization. This could lead to failure of learning due to an unbalanced MSE loss, where a small number of high-intensity pixels contribute to most of the training losses, making training difficult. This impact becomes significant when the actual signal is low. To address this issue, we clipped the acquired image data to the 0.005~99.995 percentile of the data distribution, narrowing down the lower and upper ends. We found this simple trick drastically improved the network robustness across all the microscope images we collected, while having a negligible impact on the actual data. We implemented this technique for real-world microscopy images and standardized our protocol when comparing with different methods.

Striping noise is a common artefact in HSI due to the nature of how hyperspectral images are acquired: wavelength-specific images of a sample are obtained through line scans, where calibration errors and sensitivity variations of the detector can generate artefacts along the x or y direction of the image⁵.

Determine the dominant noise source: For high light condition (i.e. high signal counts), shot noise becomes dominant and can be well approximated as Gaussian distribution. For low light, both thermal and shot noises can be dominant. However, the camera in our hyperspectral setup operates at room temperature, thus thermal noise has greater impact than shot noise, and thus we are able to assume most of the noise can be modeled as Gaussian. On the other hand, our network can be fine-tuned with any noise type by simply pre-processing the image with a given noise model. For simplicity, we use additive Gaussian noise to prepare the training data, and we demonstrate that our model is able to remove other noise types (such as striping noise) in addition to Gaussian noise when compared with the high-quality ground truth image (**Extended Data Fig. 3**). We note a well-estimated noise model close to real world situation is likely to further improve the results.

Supplementary Note 2: Training data and data collection guidelines

In non-blind image denoising, our noisy data is simulated and thus automatically labelled without human annotation. The size of the clean image is $1280 \times 303 \times 191$. We only used the first 32 channels to create the dataset, where the original image is segmented along the width dimensions with a ratio of 2:1:1 to prepare the training, validation, and testing sets. Only one noisy image is generated at a given noise level and paired with the clean image for training.

In blind denoising, we collected real-world microscopy data, and one noisy image was captured for each camera exposure setting. To denoise a single noisy image, we fine-tuned the algorithm by learning to denoise a noisier version of this image with additional Gaussian noise. We used 4 automatically generated noisier images, each at a given noise level of $\sigma = 5, 10, 20, \text{ and } 50$. We utilized the pretrained model from the previous non-blind application and fine-tuned the model for the best

performance. For this purpose, we used two real-world images: one from the publicly-available remote-sensing dataset and one from the current input.

We note that increasing the amount of training data may further improve the model performance (Supplementary Table 2). However, it would require i) ensuring consistent lighting and sample conditions throughout the data collection period, and ii) uniformity in sample morphology and optical properties across the sampled regions. Given these challenges, we have chosen to utilize datasets that contain only one target image.

Supplementary Note 3: Evaluation metrics

Besides visual comparisons, four quantitative evaluation metrics were used to analyze the results of different non-blind denoising methods: peak signal-to-noise ratio (PSNR), structural similarity index measure (SSIM)⁶, spectral angle mapper (SAM)⁷ and relative dimensionless global error synthesis (erreur relative globale adimensionnelle de synthese, ERGAS)⁸. SAM and ERGAS are metrics designed for HSI data. SAM quantifies the pixel-wise spectral distortion of two spectra, and ERGAS measures the global distortion of two hyperspectral images.

Peak signal-to-noise ratio: The PSNR is widely used to quantify the quality of images and videos subject to noise corruption. It is a full reference metric that requires an initial noise-free image as the reference. It is a variation of the mean square error (MSE) and focuses on pixel-to-pixel comparison. For a hyperspectral image $I \in \mathbb{R}^{W \times H \times C}$, its MSE against the high-quality ground truth image $X \in \mathbb{R}^{W \times H \times C}$ can be calculated as

$$\text{MSE} = \frac{1}{WHC} \sum_{i=0}^{W-1} \sum_{j=0}^{H-1} \sum_{c=0}^{C-1} [I(i, j, c) - X(i, j, c)]^2$$

The PSNR can be defined as

$$\begin{aligned} \text{PSNR} &= 10 \cdot \log_{10} \left(\frac{\max(\mathbf{X})^2}{\text{MSE}} \right) \\ &= 20 \cdot \log_{10}(\max(\mathbf{X})) - 10 \cdot \log_{10}(\text{MSE}) \end{aligned}$$

where $\max(\mathbf{X})$ represents the maximum pixel value of the image \mathbf{X} . For example, the maximum pixel value in an 8-bit RGB image is 255. The PSNR score increases as the MSE between the noisy and the reference image is reduced, and it reaches ∞ when two identical images are used.

Structural similarity index measure: The SSIM is a full reference metric used to quantify the perceived quality of images and videos by measuring the similarity between the noisy and the reference images. The main difference between SSIM and PSNR is that the PSNR measures pixel-to-pixel absolute errors, while SSIM estimates the inter-dependencies among spatially-closed pixels that carry crucial visual information about the structure of the objects. The calculation of SSIM involves three comparison functions: luminance (l), contrast (c), and structure (s):

$$\begin{aligned} l &= \frac{2\mu_I\mu_X + c_1}{\mu_I^2 + \mu_X^2 + c_1} \\ c &= \frac{2\sigma_I\sigma_X + c_2}{\sigma_I^2 + \sigma_X^2 + c_2} \\ s &= \frac{\sigma_{IX} + c_3}{\sigma_I\sigma_X + c_3} \end{aligned}$$

where μ is the pixel mean of an image, σ^2 is variance of an image, σ_{IX} is the covariance of image σ_I and high-quality reference image \mathbf{X} , $c_1 = (k_1L)^2$, $c_2 = (k_2L)^2$, and $c_3 = c_2/2$ are three variables to avoid instability of the division where the mean or standard deviation is close to zero, L is the data range of the pixel value, and $k_1 = 0.01$ and $k_2 = 0.03$ are normal constants and set by default values in SSIM calculation.

SSIM is the weighted combination of the above comparison functions

$$\text{SSIM} = l^\alpha \cdot c^\beta \cdot s^\gamma$$

where the weight α , β , and γ are set to 1. Thus, the calculation of SSIM can be simplified as

$$SSIM = \frac{(2\mu_I\mu_X + c_1)(2\sigma_I\sigma_X + c_2)}{(\mu_I^2 + \mu_X^2 + c_1)(\sigma_I^2 + \sigma_X^2 + c_2)}$$

The SSIM score increases from 0 to 1 as the structural similarity between the noisy and the reference image increases, and it reaches 1 when two identical images are used.

Spectral angle mapper: The SAM is a full reference metric that measures the local spectral similarity between noisy and reference spectra. Given a test spectrum t and a reference spectrum r of length C , the SAM is calculated as

$$SAM = \cos^{-1} \left(\frac{\sum_{c=1}^C t_c r_c}{\sqrt{\sum_{c=1}^C t_c^2} \sqrt{\sum_{c=1}^C r_c^2}} \right)$$

where c is the index for each band. The SAM score decreases as the spectral similarity between the noisy and the reference spectrum increases and reaches 0 when two identical spectra are used.

Relative dimensionless global error synthesis: The ERGAS index is a full reference metric that evaluates the global distortion between the noisy and the reference hyperspectral images by calculating the average MSE with additional weightage of the signal intensity of wavelength-specific images. If the two images have the same spatial resolution, then the ERGAS index is calculated as

$$ERGAS = 100 \sqrt{\frac{1}{C} \sum_{c=1}^C \frac{MSE(I_c, X_c)}{\mu(X_c)^2}}$$

where C denotes the number of spectral bands, c denotes the index for each band, $MSE(I_c, X_c)$ is the MSE for c -band between the noisy and the reference image, and $\mu(X_c)$ is the mean of c -band of the reference image. The ERGAS index decreases as the global similarity between the noisy and the reference spectra increases, and it reaches 0 when two identical images are used.

Supplementary Note 4: Model network interpretation

To demonstrate the effects of noise padding of PA-Net, we extracted the output feature maps of the first BN layer and took the average activation output of each filter while the noise level varied from low ($\sigma = 5$) to high ($\sigma = 75$). **Extended Data Fig. 2** illustrated that the feature map activation of PA-Net had a wider distribution than that of PA-CNN, indicating the addition of a noise sensor improved the model sensitivity to noise-level changes. The feature maps were either activated or suppressed as the noise level increased. We avoided the overwhelming contribution of padding layer values by normalizing them before feeding them into the network, which ensured that the feature map activations were not purely contributed by large input values. The smooth transition of feature map activation in PA-Net from $\sigma = 5$ to 75 demonstrated that PA-Net could carry out noise-level-aware denoising given the noise level detected by the noise detector. This further explained the performance improvement of our proposed PA-Net in dealing with different noise levels by incorporating the noise padding strategy (**Extended Data Fig. 3**).

Supplementary Note 5: Calculating signal-to-noise ratio of hyperspectral images

The signal-to-noise ratio (SNR) of a 3D hyperspectral image can be calculated in two ways: i) we can treat 3D data as a set of 2D greyscale images and calculate the SNR of the 2D image at a given wavelength channel c , or ii) we can treat 3D data as a set of 1D spectrum signals and calculate the SNR for a given spatial pixel (x, y) . The SNR is thus calculated as the mean μ of the data divided by the standard deviation σ of a human-labelled background region:

$$\text{i) } SNR_c = \frac{\mu_{2D \text{ image}}}{\sigma_{background}} \quad \text{or} \quad \text{ii) } SNR_{x,y} = \frac{\mu_{spectrum}}{\sigma_{background}}$$

Supplementary Note 6: Calculating effective photons from CCD readings

The photons detected by a CCD camera are converted into the number of electrons (e^-) in analog-to-digital units (ADU) or counts. The full well capacity of our microscope camera (i.e. the maximum e^- per pixel) is 30,000 electrons, corresponding to the maximum counts on the camera ($2^{16} = 65,536$). 1 photon detected by the camera is converted into 1 electron, and the intensity of 20,000 counts in a pixel corresponds to $20,000/2^{16} \times 30,000 = 9155$ photons, leading to a CCD gain value of 2.18. Not all photons reaching the camera are detected, and the quantum efficiency of the camera depends on the wavelength. As image quality is only affected by detected photons, not the received photons, we do not need to consider the quantum efficiency conversion of the detector when evaluating the image quality.

Supplementary Note 7: Deriving ground truth of PL spectrum in micro-PL mapping

The spatial resolution of a well-calibrated optical microscope can be estimated with the Abbe diffraction limit⁹,

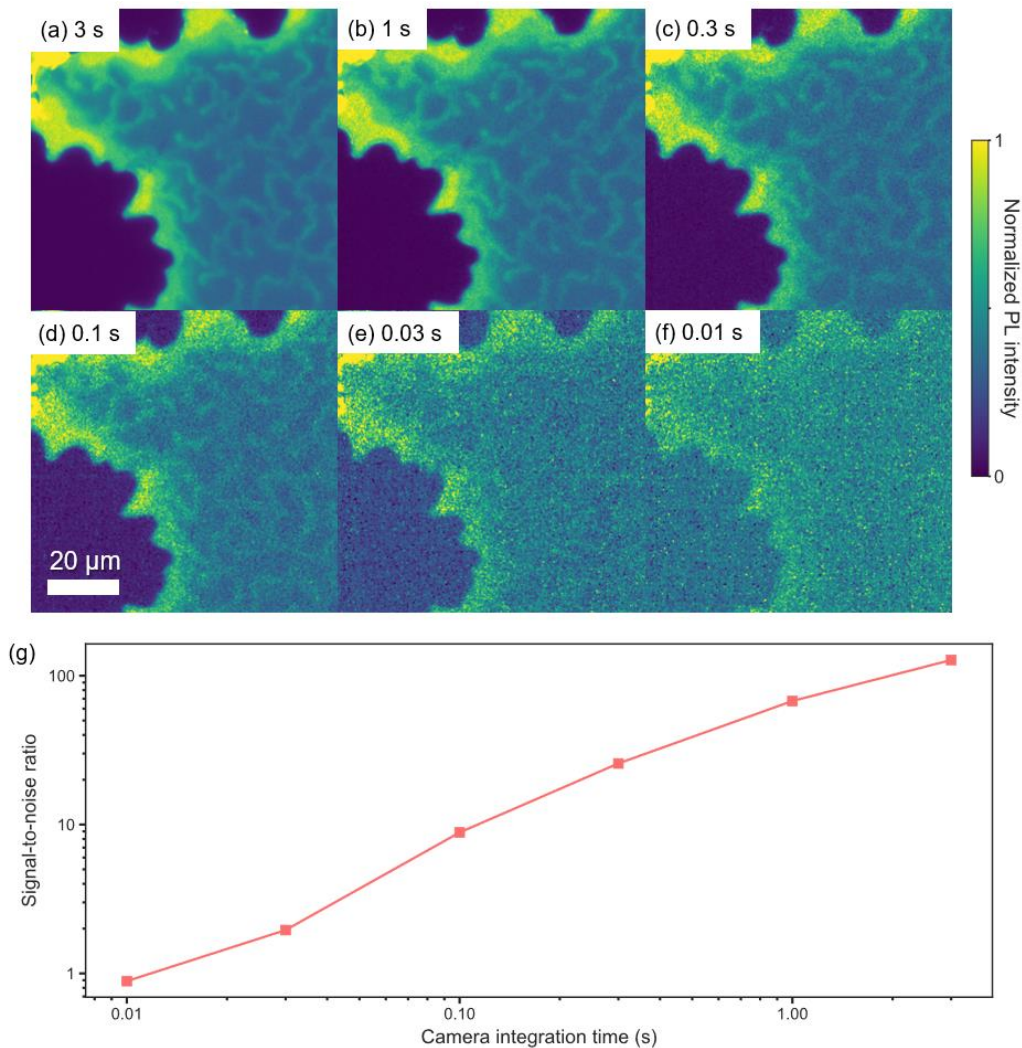
$$d = \frac{\lambda}{2n \sin\theta} = \frac{\lambda}{2NA}$$

where λ is the wavelength of light, n is the refractive index of the medium, θ is the half aperture angle in radians, and NA is the numerical aperture of the objective lens.

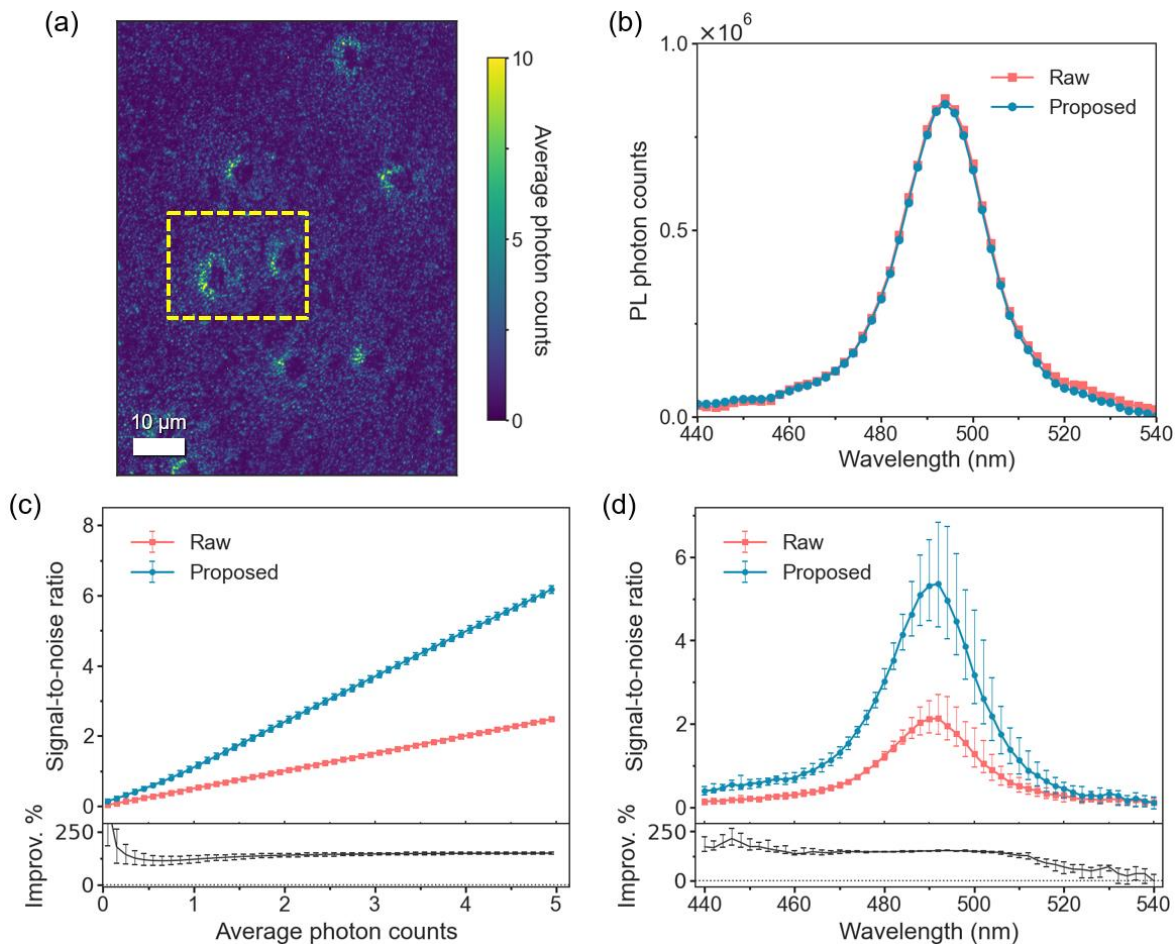
We used Nikon CFI Plan Fluor 20x objective lens with a NA of 0.45. With an incident PL emission ranging from 440 to 540 nm, our best spatial resolution is calculated as ~ 600 nm. However, the spatial distance of each pixel in the data cube was 330 nm, suggesting that some of the spectral signals from surrounding pixels had been merged into that of the current one, resulting in mixing of the spectrum among adjacent pixels.

Thus, we could sum up the spectrum signals of a total number of x^2 pixels with size (x, x) into the one pixel through pixel binning, sacrificing the digital resolution of the image by x times, by assuming that the spectrum signals came from a single emission source. With the digital resolution halved ($x = 2$),

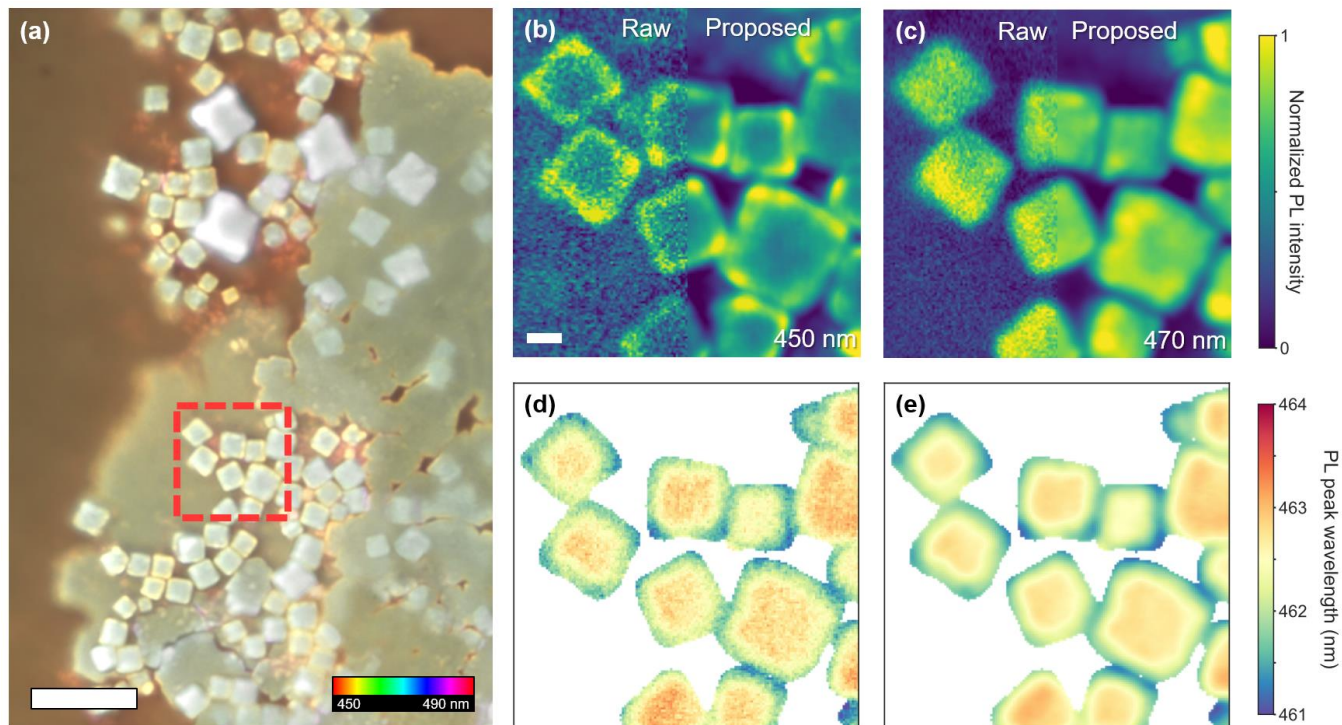
the spectral signal of a pixel is improved by fourfold and the SNR is improved by twofold¹⁰, and thus the spectrum of previously noisy pixels could now be fitted closer to the unmeasurable ground truth. We note this is a rough and simple approach, experimentally equivalent to having a measurement of the given sample with a 10x objective lens under identical conditions.



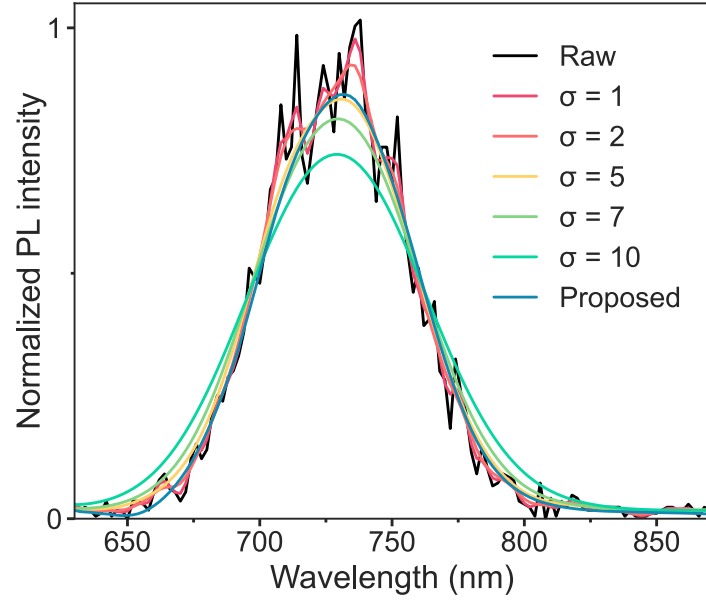
Supplementary Figure 1. Effect of background noise levels in human visual signal detection of small features. **a-f**, Normalized PL intensity maps of a photostable organic film, mCBP-doped 4CzIPN, at 560 nm with different camera integration times of **(a)** 3 s, **(b)** 1 s, **(c)** 0.3 s, **(d)** 0.1 s, **(e)** 0.03 s and **(f)** 0.01 s. The sample was excited under a 405 nm CW laser with a power intensity of 100 mW cm^{-2} . Scalebar is 20 μm . **g**, The signal-to-noise ratios of the images versus different camera integration time settings.



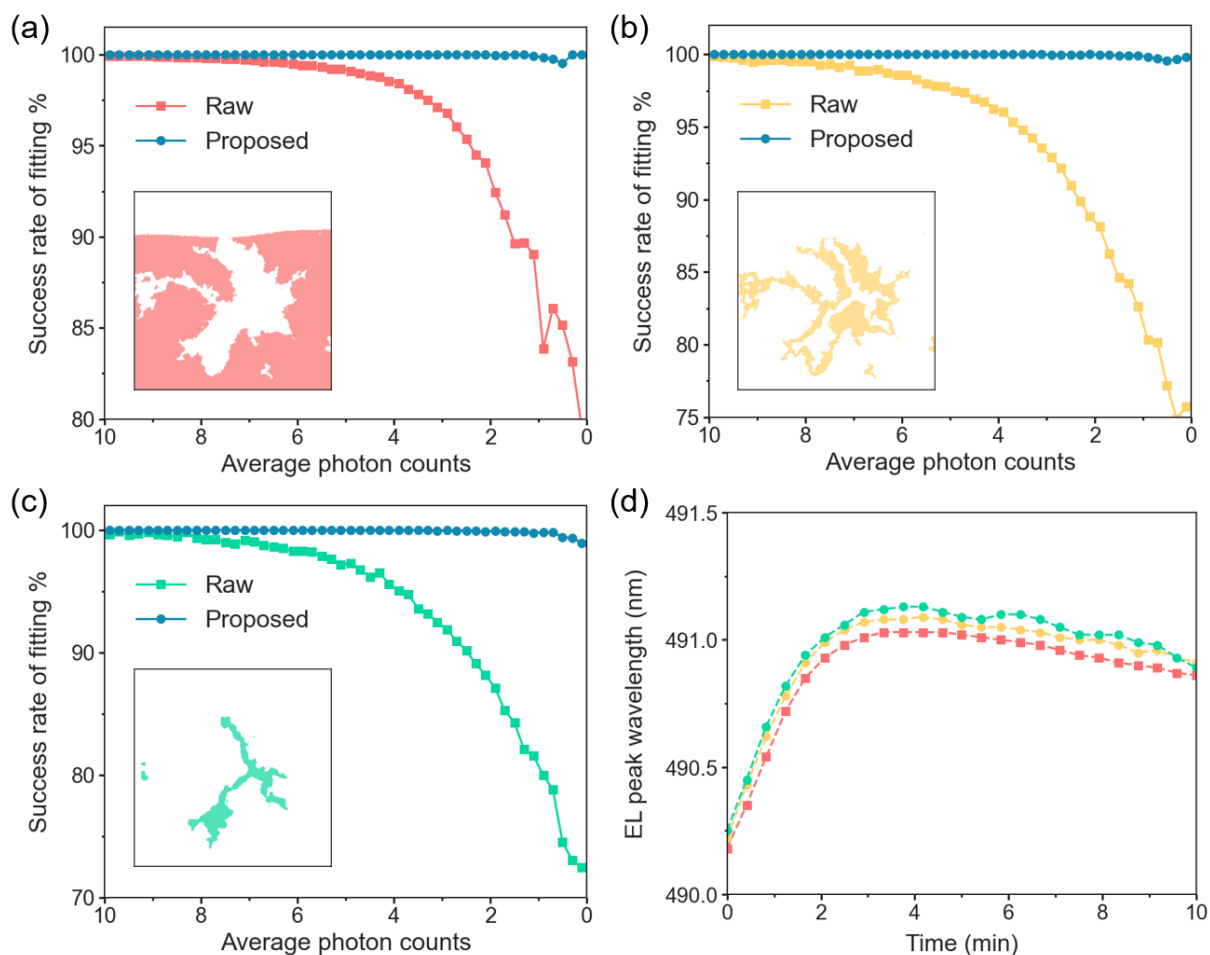
Supplementary Figure 2. Hyperspectral microscopy of CsPbBr₃ perovskite nanoplatelets. **a**, Raw PL intensity map averaged across wavelengths. **b**, Sum of the PL spectrum of the indicated zone in **(a)** for raw and denoised images. **c,d**, Statistics of signal-to-noise ratio (SNR) (above) and the percentage improvement (below) after image restoration with respect to average photon counts of the pixel **(c)** or per wavelength-specific image **(d)**. The statistics was calculated from evenly-cropped subzones (sample size $n = 100$) of the original image in **a**. The percentage improvements are presented as median values with the error bar of the lower and upper quartile. The signal-to-noise ratio was calculated using the mean of the signal intensity divided by the standard deviation of the background region where no perovskite signal was captured.



Supplementary Figure 3. Hyperspectral microscopy of CsPbBr₃ perovskite nanosheets. **a**, Micro-sized CsPbBr₃ nanosheet film after denoising. Images are color-coded using ImageJ Fiji software to indicate spectral intensity. **b,c**, Normalized PL intensity map at **(b)** 450 nm and **(c)** 470 nm. **d,e**, The raw **(d)** and processed **(e)** local PL peak maps of the nanosheets. The Gaussian function was used to fit the local PL curve for each pixel, and the peak position was found at the maximum of the fitted spectra. Scalebars are 10 μm in **a** and 1 μm in **b-e**.



Supplementary Figure 4. Effect of 1D Gaussian filter on local-PL spectra of wide-gap $\text{FA}_{0.7}\text{Cs}_{0.3}\text{Pb}(\text{I}_{0.6}\text{Br}_{0.4})_3$ perovskite films. The output PL spectra deviated when the standard deviation for Gaussian kernel, a mandatory human-inputted parameter to implement the Gaussian filter, was changed from 1 to 10.



Supplementary Figure 5. Curve fitting for EL maps of mixed Br/Cl blue perovskite LEDs. a-c, Success rate of fitting against the average EL counts of a pixel. Inset shows the corresponding zones for statistical analysis. **d,** EL peak evolution of different zones under voltage bias of 6 V for 10 min. The lines represent the median of the distributions. See **Fig. 4H** for the peak distribution of each zone.

Number of channels	Metrics	Noisy	BM4D	LLRT	QRNN3D	PA-Net
3	PSNR	13.44	27.99	26.78	27.48	29.16
	SSIM	0.1076	0.6844	0.6416	0.6736	0.7495
	SAM	0.5216	0.1089	0.126	0.1158	0.0954
	ERGAS	6841	1104	1221	1195	975
	Training time (h)	N/A	N/A	N/A	1.062	7.015
	Process time (s)	N/A	9.354	315	0.048	0.136
8	PSNR	14.59	30.96	29.10	27.81	31.96
	SSIM	0.1255	0.812	0.7249	0.6527	0.8498
	SAM	0.5262	0.0858	0.1107	0.129	0.0799
	ERGAS	11400	1594	1880	2354	1332
	Training time (h)	N/A	N/A	N/A	2.362	7.129
	Process time (s)	N/A	11.23	299	0.126	1.956
16	PSNR	17.92	33.31	32.54	32.07	35.88
	SSIM	0.1824	0.8706	0.8332	0.8144	0.926
	SAM	0.5113	0.0896	0.1005	0.1054	0.0692
	ERGAS	16008	2482	2613	3755	1757
	Training time (h)	N/A	N/A	N/A	3.995	7.333
	Process time (s)	N/A	29.5	11497	0.297	2.107
24	PSNR	18.29	33.46	33.18	30.76	36.52
	SSIM	0.2199	0.8844	0.869	0.8124	0.9453
	SAM	0.4953	0.0897	0.0925	0.125	0.0637
	ERGAS	19419	3095	3128	4445	2063
	Training time (h)	N/A	N/A	N/A	6.884	7.596
	Process time (s)	N/A	77.54	6101	0.328	1.533
32	PSNR	18.74	33.59	33.87	30.43	36.94
	SSIM	0.2537	0.894	0.8979	0.7788	0.9581
	SAM	0.4844	0.0908	0.0872	0.1338	0.0621
	ERGAS	22515	3736	3648	5678	2410
	Training time (h)	N/A	N/A	N/A	9.044	8.179
	Process time (s)	N/A	179.8	4959	0.437	3.521

Supplementary Table 1. Evaluation of model generalizability with different number of channels of the input image ($\sigma = 20$). The dataset was prepared by cropping the first n channels from the original HYDICE DC Mall image. QRNN3D and PA-Net were trained with multiple noise levels ($\sigma = 10, 20$, and 50). BM3D and LLRT were performed on laptop CPU (Intel Core i9-12900H) while QRNN3D and PA-Net were performed on a GPU core (NVIDIA Tesla P100).

Metrics	Amount of training data (%)						
	100	75	50	25	18	10	5
PSNR	36.94	36.73	35.97	34.67	32.48	29.84	29.20
SSIM	0.9581	0.9565	0.9508	0.9432	0.9332	0.9165	0.9036
SAM	0.0621	0.0636	0.0695	0.08	0.0996	0.1332	0.1487
ERGAS	2410	2447	2645	2886	3292	4153	4314

Supplementary Table 2. Effect of training data percentage on denoised image quality and accuracy metrics. A consistent deterioration in image quality, similarity, and accuracy metrics is observed as the percentage of training data decreases. This suggests that a larger training data size may lead to improved model performance in image restoration.

Metrics	Patch size							
	64	32	16	12	10	8	6	4
PSNR	36.94	37.09	37.42	37.10	36.21	28.20	20.22	10.48
SSIM	0.9581	0.9576	0.9611	0.9592	0.9554	0.9315	0.5239	0.3556
SAM	0.0621	0.0613	0.0588	0.0606	0.0652	0.0957	0.3859	0.5213
ERGAS	2410	2405	2304	2446	2864	7880	18127	60663
Detector modification	/	/	-1 conv layer	-1 conv layer	-2 conv layer	-2 conv layer	-3 conv layer	-3 conv layer

Supplementary Table 3. Effect of patch size on denoised image quality and accuracy metrics. The total amount of layers in the detector network was slightly reduced to adjust the patch size change. There is an optimal patch size range (around 12 to 32) that balances image quality improvement and preservation of relevant features. Beyond this range, both image quality and accuracy metrics might start to deteriorate due to loss of local details (larger patches) or information loss (smaller patches).

Image size	Time cost	Noise2Void	Noise2Fast	Self2Self	PA-Net
400×400×176 (15%)	Training (h)	0.330	10.946	4.804	2.104
	Process (s)	23.78	N/A	N/A	7.672
	Total (h)	0.337	10.946	4.804	2.106
1024×1024×88 (50%)	Training (h)	0.842	44.349	24.539	2.115
	Process (s)	OOM	N/A	N/A	74.77
	Total (h)	N/A	44.349	24.539	2.136
1024×1024×176 (full size)	Training (h)	OOM	90.008	OOM	1.856
	Process (s)	N/A	N/A	N/A	184.4
	Total (h)	N/A	90.008	N/A	1.907

Supplementary Table 4. Evaluation on blind denoising processing speed for each method with various input image size. The algorithms were run on a single Tesla P100 GPU with 16 GB memory. For Noise2Fast and Self2Self, no additional processing is required after the last training step. OOM: out of memory.

Supplementary References

1. Rasti, B., Scheunders, P., Ghamisi, P., Licciardi, G. & Chanussot, J. Noise Reduction in Hyperspectral Imagery: Overview and Application. *Remote Sensing* **10**, 482 (2018).
2. Boncelet, C. Image Noise Models. in *The Essential Guide to Image Processing* 143–167 (Elsevier, 2009). doi:10.1016/B978-0-12-374457-9.00007-X.
3. Rosenblatt, M. A Central Limit Theorem and a Strong Mixing Condition. *Proc. Natl. Acad. Sci. U.S.A.* **42**, 43–47 (1956).
4. van Dokkum, P. G. Cosmic-Ray Rejection by Laplacian Edge Detection. *PUBL ASTRON SOC PAC* **113**, 1420–1427 (2001).
5. Gómez-Chova, L. *et al.* Correction of systematic spatial noise in push-broom hyperspectral sensors: application to CHRIS/PROBA images. *Appl. Opt.* **47**, F46 (2008).
6. Wang, Z., Bovik, A. C., Sheikh, H. R. & Simoncelli, E. P. Image Quality Assessment: From Error Visibility to Structural Similarity. *IEEE Trans. on Image Process.* **13**, 600–612 (2004).
7. Boardman, J. W. Automating spectral unmixing of AVIRIS data using convex geometry concepts. in *JPL, Summaries of the 4th Annual JPL Airborne Geoscience Workshop. Volume 1: AVIRIS Workshop* (1993).
8. Wald, L. *Data fusion: definitions and architectures: fusion of images of different spatial resolutions.* (Presses des MINES, 2002).
9. Lipson, A., Lipson, S. G. & Lipson, H. *Optical Physics.* (Cambridge University Press, 2010). doi:10.1017/CBO9780511763120.
10. Rowlands, R. *Physics of Digital Photography (Second Edition).* (IOP Publishing Ltd, 2020). doi:10.1088/978-0-7503-2558-5.
11. Guo, S., Yan, Z., Zhang, K., Zuo, W. & Zhang, L. Toward Convolutional Blind Denoising of Real Photographs. in *2019 IEEE/CVF Conference on Computer Vision and Pattern Recognition (CVPR)* 1712–1722 (IEEE, 2019). doi:10.1109/CVPR.2019.00181.